# Porphyrin-Based Covalent Organic Frameworks Anchoring Au Single Atoms for Photocatalytic Nitrogen Fixation

Ting He[†,¥], Zhanfeng Zhao[‡,¶,¥], Ruoyang Liu[§], Xinyan Liu[Δ], Bing Ni[&], Yanping Wei[#], Yinglong Wu[†], Wei Yuan[†], Hongjie Peng[Δ], Zhongyi Jiang[‡,¶,$]* and Yanli Zhao[†]*

[†]School of Chemistry, Chemical Engineering and Biotechnology, Nanyang Technological University, Singapore 637371, Singapore

[‡]Key Laboratory for Green Chemical Technology of Ministry of Education, School of Chemical Engineering and Technology, Tianjin University, Tianjin 300072, P. R. China

[§]Department of Chemistry, Faulty of Science, National University of Singapore, Singapore 117543, Singapore

[Δ]Institute of Fundamental and Frontier Sciences, University of Electronic Science and Technology of China, Chengdu 611731, P. R. China

[&]Physical Chemistry, University of Konstanz, Universitätsstrasse 10, 78457 Konstanz, Germany

[#]College of Science, Gansu Agricultural University, Lanzhou 730070, P. R. China

[¶]Collaborative Innovation Center of Chemical Science and Engineering, Tianjin 300072, P. R. China

[$]Joint School of National University of Singapore and Tianjin University, International Campus of Tianjin University, Fuzhou, 350207, P. R. China

**Abstract**. The development of efficient photocatalysts for $N_2$ fixation to produce $NH_3$ under ambient conditions remains a great challenge. Since covalent organic frameworks (COFs) possess the predesignable chemical structures, good crystallinity and high porosity, it is highly significant to explore their potential for photocatalytic nitrogen conversion. Herein, we report a series of isostructural porphyrin-based COFs loaded with Au single atoms (COFX-Au, X = 1-5) for photocatalytic $N_2$ fixation. The porphyrin building blocks act as the docking sites to immobilize Au single atoms as well as light-harvesting antennae. The microenvironment of Au catalytic center is precisely tuned through controlling the functional groups at the proximal and distal position of porphyrin units. As a result, COF1-Au decorated with strong electron-withdrawing groups exhibits a high activity toward $NH_3$ production with rates of 333.0±22.4 μmol $g^{-1}$ $h^{-1}$ and 37.0±2.5 mmol $g_{Au}^{-1}$ $h^{-1}$, which are 2.8-fold and 171-fold higher than that of COF4-Au decorated with electron-donating functional groups and porphyrin-Au molecular catalyst, respectively. The $NH_3$ production rates could be further increased to 427.9 ±18.7 μmol $g^{-1}$ $h^{-1}$ and 61.1±2.7 mmol $g_{Au}^{-1}$ $h^{-1}$ under the catalysis of COF5-Au featuring two different kinds of strong electron-withdrawing groups. The structure-activity relationship analysis reveals that the introduction of electron-withdrawing groups facilitates the separation and transportation of photogenerated electrons within the entire framework. This work manifests that the structures and optoelectronic properties of COF-based photocatalysts can be finely tuned through a rational predesign at the molecular level, thus leading to the superior $NH_3$ evolution.

## Introduction

Ammonia ($NH_3$) is crucial to the sustainable development of human society owing to the indispensable role in fertilizer production, as well as being as important energy storage medium and carbon-free energy carrier.[1,2] Traditionally, $NH_3$ is produced through the Haber-Bosch process by the reaction of $H_2$ and $N_2$ under high temperature (573-773K) and high pressure (100-200 atm). Moreover, the large amount of $H_2$ required in this process accounts for nearly 1.5% of $CO_2$ released into the environment each year.[3,4] Therefore, the development of green and sustainable approaches to efficiently produce $NH_3$ under mild conditions is highly desirable.

Enlightened by natural photosynthesis that converts solar energy into chemical energy in the form of chemical bonds, photocatalytic $N_2$ reduction reaction displays the potential to produce $NH_3$ through the utilization of clean and inexhaustible sunlight.[5-8] Conventional photocatalysts including metal oxides and sulfides,[9] bismuth oxyhalides,[10] and $C_3N_4$ structures[11] have been investigated for $N_2$ reduction. However, the efficiency is still low due to the lack of sufficient active sites to bind and cleave the strong nonpolar N≡N triple bond (941 kJ $mol^{-1}$). The emerging single-atom catalysts[12-14] benefit from the advantages of distinct active sites and the maximum atom efficiency. Nevertheless, it is still challenging to precisely control the local environment of active sites.[15-17]

Two-dimensional COFs (2D COFs)[18-22] are a type of porous polymers with high crystallinity, allowing unique incorporations of photoactive organic species into 2D periodic frameworks with ordered pores for a wide range of photocatalytic reactions to take place.[23,24] The organic units aligned into crystalline 2D π lattices in semiconducting COFs can act as

pathways to facilitate the charge transport and separation, and prevent the recombination of charge carriers.[25] The porous structures with one-dimensional polygon channels are beneficial for the mass transport as well as the enrichment of feed gas.[26] Furthermore, the specific geometric and chemical structures of COFs render them ideal platforms to anchor single atoms with well-defined coordination environment, meanwhile the microenvironment of catalytic centers can be precisely tuned at the molecular level through the bottom-up strategy with predesigned building blocks. Last but not the least, the photosensitizers and co-catalysts are easily assembled into a single system simultaneously due to the predesignability and integrity of COFs as compared to the conventional photocatalysts. In brief, the development of COF catalysts to boost the photocatalytic nitrogen reduction activity is promising and important in the field.

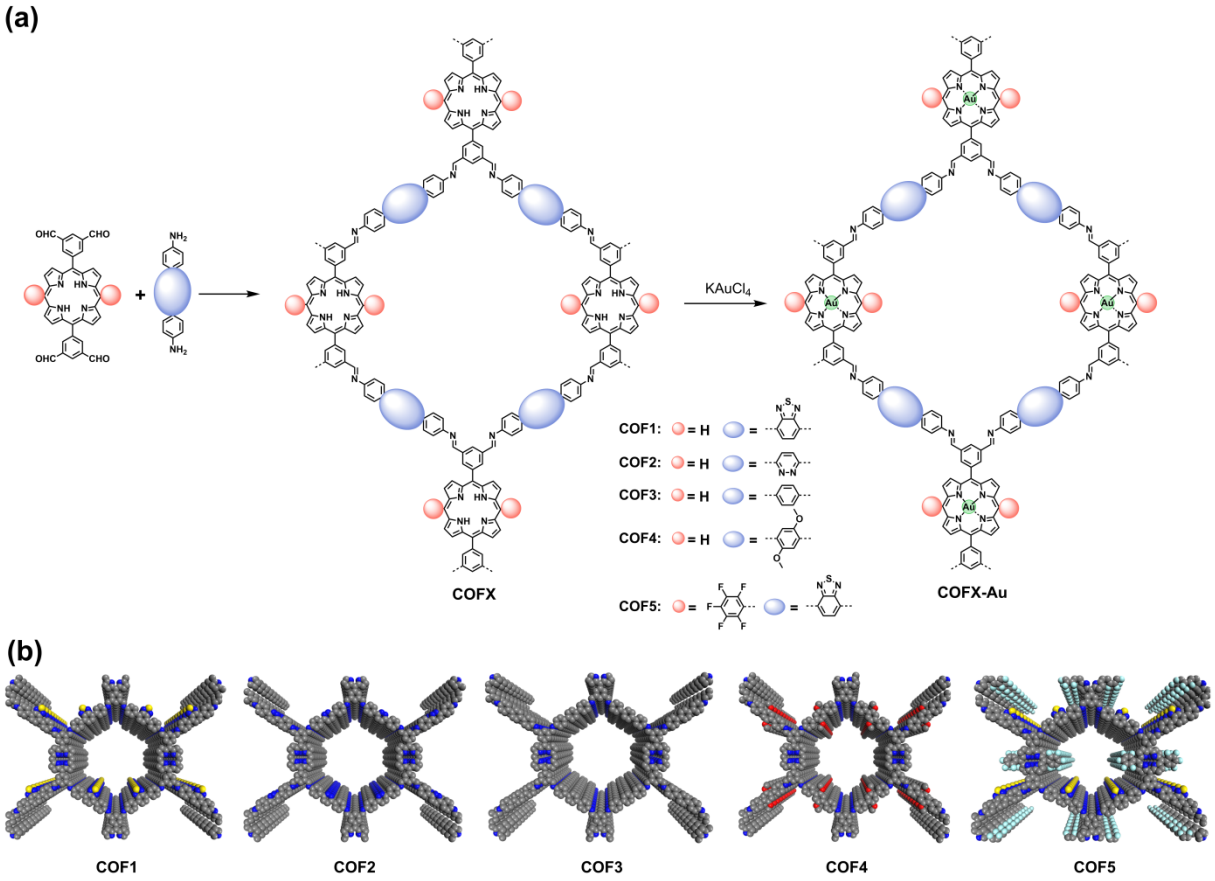

**Figure 1** Design strategy. (a) Synthetic strategy of COFX and COFX-Au. (b) Top views of COFX with ten layers (X=1-5; grey, C; blue, N; red, O; yellow, S; cyan, F).

Inspired by the biological molecule chlorophyll in green leaves, we designed a new $D_2$-symmetric porphyrin monomer as the photosensitizer to construct COFs for light harvesting. Compared to the reported $D_4$-symmetric porphyrin units (Figure S1, left), the microenvironment of catalytic sites embedded in the $D_2$-symmetric porphyrin cycles (Figure S1, right) is finely tuned through introducing electron-withdrawing and electron-donating groups at proximal position as well as distal position. Moreover, the functional groups on proximal position are expected to show stronger effect on the catalytic sites due to the shorter distance. Herein, we synthesized a series of isostructural porphyrin-based COFs (COFX, X = 1-5) with different groups at the distal position (benzothiadiazole, pyrazine, benzene, or dimethoxybenzene) and proximal position (hydrogen or pentafluorobenzene) of porphyrin units (Figure 1a). All these COFs present sql topologies with ordered 1D channels (Figure 1b). Subsequently, Au single atoms are successfully immobilized on the well-defined square-planar anchoring sites of porphyrin units (Figure 1a), which were studied by synchrotron-radiation based X-ray absorption fine-structure spectroscopy and aberration-corrected high-angle annular dark-field scanning transmission electron microscopy (HAAF-STEM). The porphyrin units could absorb light to generate electrons and holes. Then, the photogenerated electrons are transported to the Au sites to drive the $N_2$ reduction. COFX-Au (X = 1-5) with unique single-atom characteristics exhibited high performance for the photocatalytic $N_2$ reduction with a clear structure-activity correlation. The investigation on

optoelectronic properties of COFX-Au demonstrates that the strong electron-withdrawing groups could facilitate the separation and transportation of photo-induced electrons. Therefore, COF1-Au and COF5-Au equipped with strong electron-withdrawing groups on distal and proximal positions present higher $NH_3$ evolution rates of 333.0±22.2 and 427.9±18.7 μmol $g^{-1}$ $h^{-1}$ respectively, as compared to the photocatalysts with electron-donating groups. The $NH_3$ evolution rates of COF1-Au and COF5-Au are calculated to be as high as 37.0±2.5 mmol $g_{Au}^{-1}$ $h^{-1}$ and 61.1±2.7 mmol $g_{Au}^{-1}$ $h^{-1}$ respectively, which are 171 and 283 times higher than porphyrin-Au molecular catalyst. These findings afford valuable insights into the structural design of COF catalysts for photocatalytic $N_2$ fixation.

**Results and Discussion**

COF1 was successfully synthesized by the reaction of 5,5'-(porphyrin-5,15-diyl)diisophthalaldehyde (P-CHO) and 4,4'-(benzo[*c*][1,2,5]thiadiazole-4,7-diyl)dianiline (Bt-$NH_2$) in the presence of 1,2-dichlorobenzene/1-butanol (*v*/*v* = 1/1) with 6M acetic acid as a catalyst at 120 °C for 3 days (88 % yield). The replacement of amine monomer with 4,4'-(pyridazine-3,6-diyl)dianiline (Pz-$NH_2$), [1,1':4',1"-terphenyl]-4,4"-diamine (TP-$NH_2$) or 2',5'-dimethoxy-[1,1':4',1"-terphenyl]-4,4"-diamine (DMTP-$NH_2$) yielded COF2, COF3 or COF4 under similar reaction conditions. COF5 was achieved when 5,5'-(10,20-bis(perfluorophenyl)porphyrin-5,15-diyl)diisophthalaldehyde ($PF_5$-CHO) was used as the aldehyde monomer.

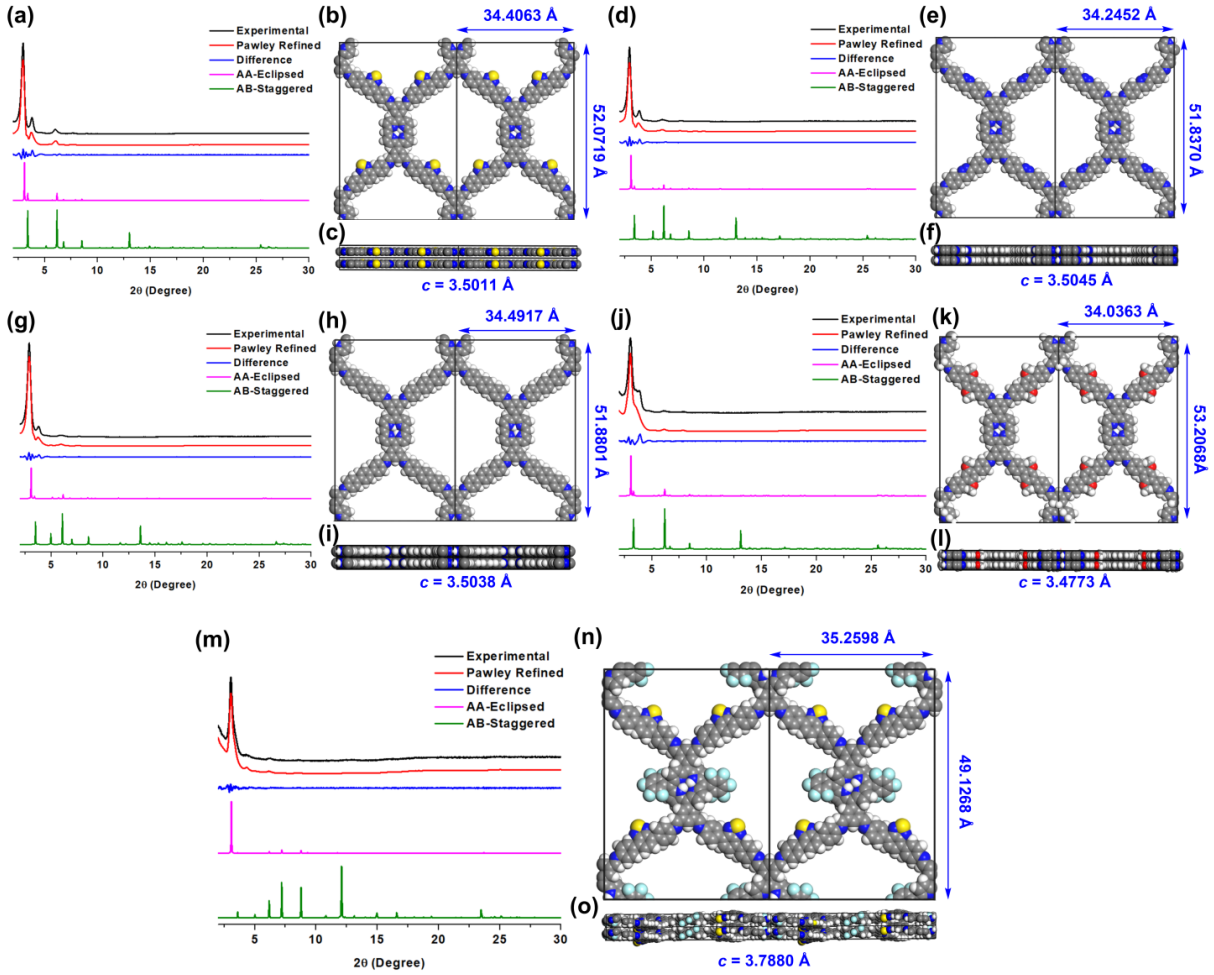


**Figure 2** X-ray diffraction and crystal structure. PXRD profiles of (a) COF1, (d) COF2, (g) COF3, (j) COF4, and (m) COF5 (black, experimental curves; red, Pawley refined; blue, their difference; purple, AA-eclipsed mode; green, AB-staggered mode). Reconstructed crystal structures of (b, top view; c, side view) COF1, (e, top view; f, side view) COF2, (h, top view; i, side view) COF3, (k, top view; l, side view) COF4, and (n, top view; o, side view) COF5 (grey, C; white, H; blue, N; red, O; yellow, S; cyan, F).

The crystalline structures of COFX were determined with powder X-ray diffraction (PXRD) by using Cu Kα radiation. The PXRD pattern of COF1 (Figure 2a, black curve) exhibited strong peaks at 3.0°, 3.8°, 6.0°, and 7.6°, assigned to (110), (020), (220), and (310) lattice

planes, respectively. The weak peak at 27.2° corresponded to (001) plane, which coincided with the π-π stacking between the two-dimensional layers. The Pawley-refined (Figure 2a, red curve) result revealed that COF1 adopted an AA-eclipsed stacking mode (Figure 2a, purple curve) rather than AB-staggered mode (Figure 2a, green curve), where AA-eclipsed curve matched well with experimental data (Figure 2a, blue curve). The COF1 adopted *P*222 group space No. 16 with the lattice parameters of $\alpha = \beta = \gamma = 90°$, $a$ = 34.4063 Å, $b$ = 52.0719 Å, and $c$ = 3.5011 Å (Figure 2b,c; Tables S1 and S6). Other COFX COFs presented similar PXRD results (Figure 2d, g, j, m) and crystalline structures (Figure 2e, f, h, i, k, l, n, o; Tables S2-S6) due to the isostructural nature. The weak π-π stacking peak of COF5 at 25.0° from (001) facet was smaller than that of COF1, revealing the larger inter-layer distance of COF5 because of the steric hindrance and repulsion of perfluorophenyl groups.

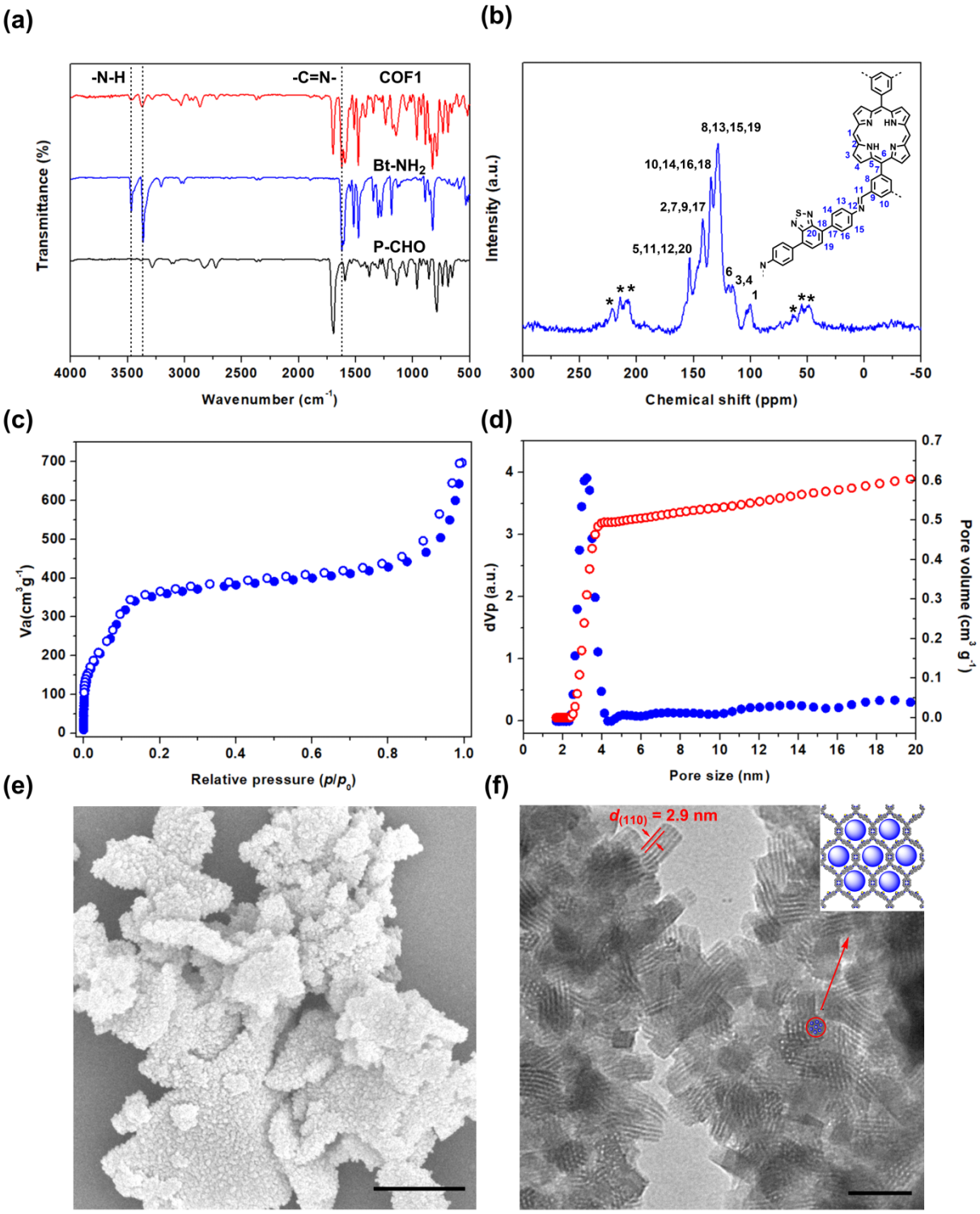


**Figure 3** Characterization of COF1. (a) FTIR spectra of P-CHO, Bt-$NH_2$ and COF1. (b) Solid-state $^{13}C$ CP/MAS NMR spectrum (asterisks indicate spinning sidebands), (c) $N_2$ sorption isotherms, (d) pore size distribution and pore volume curves, (e) SEM image (scale bar, 1 μm) and (f) TEM image (scale bar, 50 nm, inset, top view of COF1) of COF1.

Fourier-transform infrared (FTIR) spectrum of COF1 presented the disappearance of N-H stretching bands at 3400-3500 $cm^{-1}$ and the appearance of C=N stretching vibration at 1620 $cm^{-1}$, revealing the formation of imine C=N linkage (Figure 3a). The chemical structure of COF1 was further analyzed by the $^{13}C$ solid-state CP/MAS NMR spectroscopy (Figure 3b). The peak located at 116 ppm belonged to the $C_3$ and $C_4$ of pyrrole units and the signal at 99 ppm was attributed to the $C_1$ of porphyrin macrocycles. Porosity is significant for COFs in the application of catalysis for mass transport. The porosity of COF1 was studied using nitrogen adsorption/desorption isotherms at 77 K. The typical type IV isotherm suggested the mesoporous character (Figure 3c). Brunauer-Emmett-Teller (BET) surface area was calculated to be 1263 $m^2\ g^{-1}$. The pore size distribution curves (Figures 3d and S2) revealed that the pore size and pore volume of COF1 was 3.2 nm and 0.61 $cm^3\ g^{-1}$, respectively. Scanning electron microscopy (SEM) image (Figure 3e) demonstrated a particle-like morphology of COF1, while transmission electron microscopy (TEM) image (Figure 3f) displayed visualized parallel lines with a distance of 2.9 nm, attributed to the dominant (110) plane of the ordered frameworks. This result matched well with the PXRD data of COF1. Interestingly, many honeycomb-like pores (Figure 3f, red circle and inset) were clearly observed, which should be derived from the [001] direction. The thermogravimetric curves (Figure S3a) obtained under nitrogen atmosphere demonstrated high thermal stability of COF1 beyond 500 °C. The characterizations of other COFX COFs were also systematically conducted to verify their chemical structures, porosities, morphologies and thermal stabilities (Figures S3-S10).

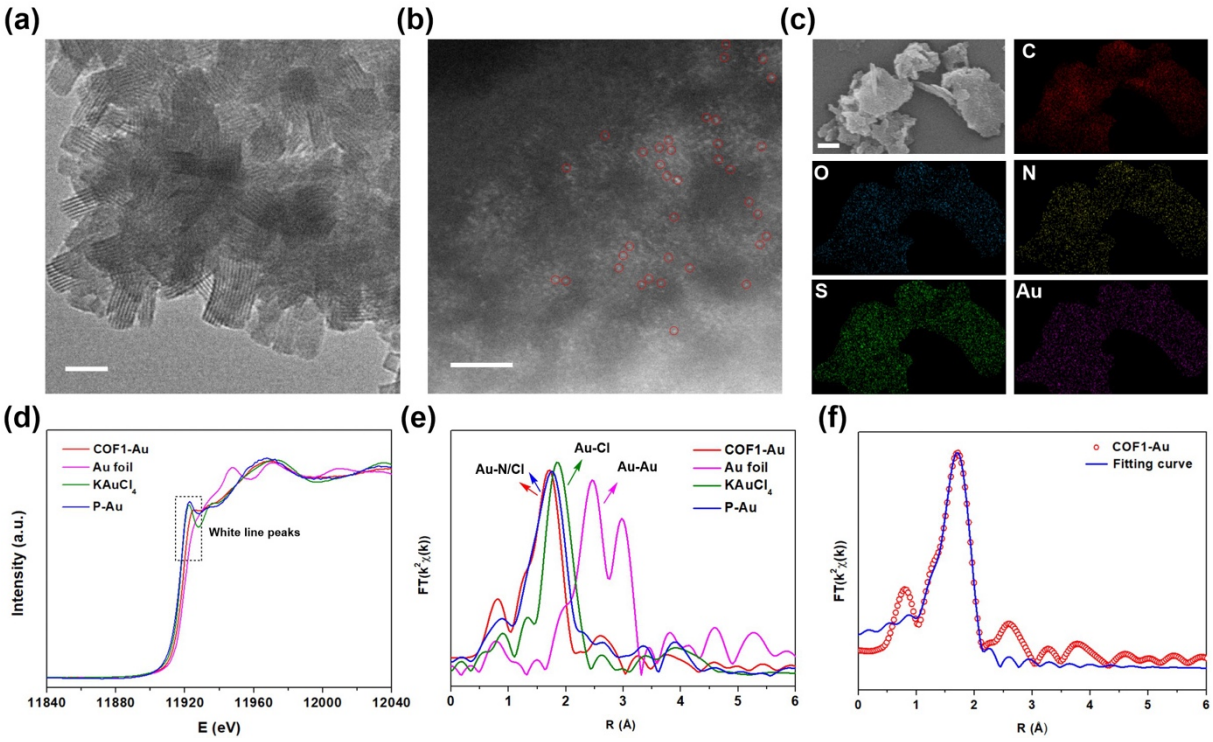


**Figure 4** Characterization of COF1-Au. (a) TEM image of COF1-Au (scale bar, 50 nm). (b) Aberration-corrected HAADF-STEM image (scale bar, 2 nm) of COF1-Au (Single Au atoms are indicated by red circles.). (c) SEM image (scale bar, 1 μm) and corresponding elemental mapping of COF1-Au. (d) Au $L_3$-edge XANES spectra and (e) FT-EXAFS spectra of COF1-Au, Au foil, $KAuCl_4$ and P-Au. (f) Corresponding EXAFS *r* space fitting curve of COF1-Au.

COF1-Au was prepared through treating COF1 with $KAuCl_4$ in *N*,*N*-dimethylformamide at 85 °C for 24 h. The crystal structure of COF1 was well retained after loading Au species according to the post-metalation PXRD pattern (Figure S11a). No peak assigned to Au particles was observed from the PXRD result (Figure S11a, inset). $N_2$ sorption analysis (Figure S12) demonstrated that the BET surface area and pore volume of COF1-Au decreased to 1230 $m^2\ g^{-1}$ and 0.6 $cm^3\ g^{-1}$ respectively, owing to the mass increment from Au species. No

detectable Au nanoparticles were observed in the TEM image (Figure 4a) of COF1-Au. To our delight, Au single atoms were observed clearly as bright spots (marked by red circles) by aberration-corrected HAADF-STEM (Figures 4b and S13). SEM elemental mapping (Figure 4c) revealed that Au was uniformly distributed over the whole COF1-Au sample. The Au content was determined to be 0.9 wt% by inductively coupled plasma optical emission spectroscopy (ICP-OES). Synchrotron-radiation-based extended X-ray absorption fine structure (EXAFS) and X-ray absorption near-edge spectroscopy (XANES) measurements were performed to further confirm the local structure of Au speciation. (5,10,15,20-Tetraphenylporphyrinato)gold (P-Au), a molecular analogue of the porphyrin-gold subunit from COF1-Au, was synthesized (see the Supporting Information for the synthesis details) for the comparison. The white line peak in the Au $L_3$-edge XANES arose from the electronic transition of Au $2p_{3/2}$ to unoccupied 5d or 6s states. Compared to Au foil with no white line peak, COF1-Au exhibited a sharp peak (Figure 4d). Moreover, the binding energy of COF1-Au (Figure 4d, red curve) located between Au foil and $KAuCl_4$ revealed the positive valence nature of Au atom in COF1-Au.[27] The Fourier transform (FT)-EXAFS curve (Figure 4e) of COF1-Au at Au $L_3$-edge showed a main peak at 1.7 Å, which might be assigned to Au-N/Cl coordination.[28] Moreover, no Au-Au (2.4 and 3.0 Å) peak was detected as compared to Au foil, confirming the single-atom nature of Au in COF1-Au. Noticeably, the P-Au exhibited an obvious peak at 1.74 Å, close to that of COF1-Au, suggesting the porphyrin-gold structure in COF1-Au. To gain the structural parameters of Au species for COF1-Au, the EXAFS fitting was conducted (Figure 4f and Table S7). The coordination numbers of Au were calculated to be 3.0 (±0.9) Au-N and 1.9 (±

0.5) Au-Cl (Table S7). As a result, it could be concluded that the Au single atoms were well coordinated by the nitrogen atoms of porphyrin units to form square-planar structures. Other COFX-Au systems were also prepared by the same method and characterized by various techniques (Figures S11 and S14-S18). The Au mass loading of COF2-Au, COF3-Au, COF4-Au and COF5-Au calculated by ICP-OES was 1.4 %, 1.3 %, 1.5 % and 0.7 %, respectively.

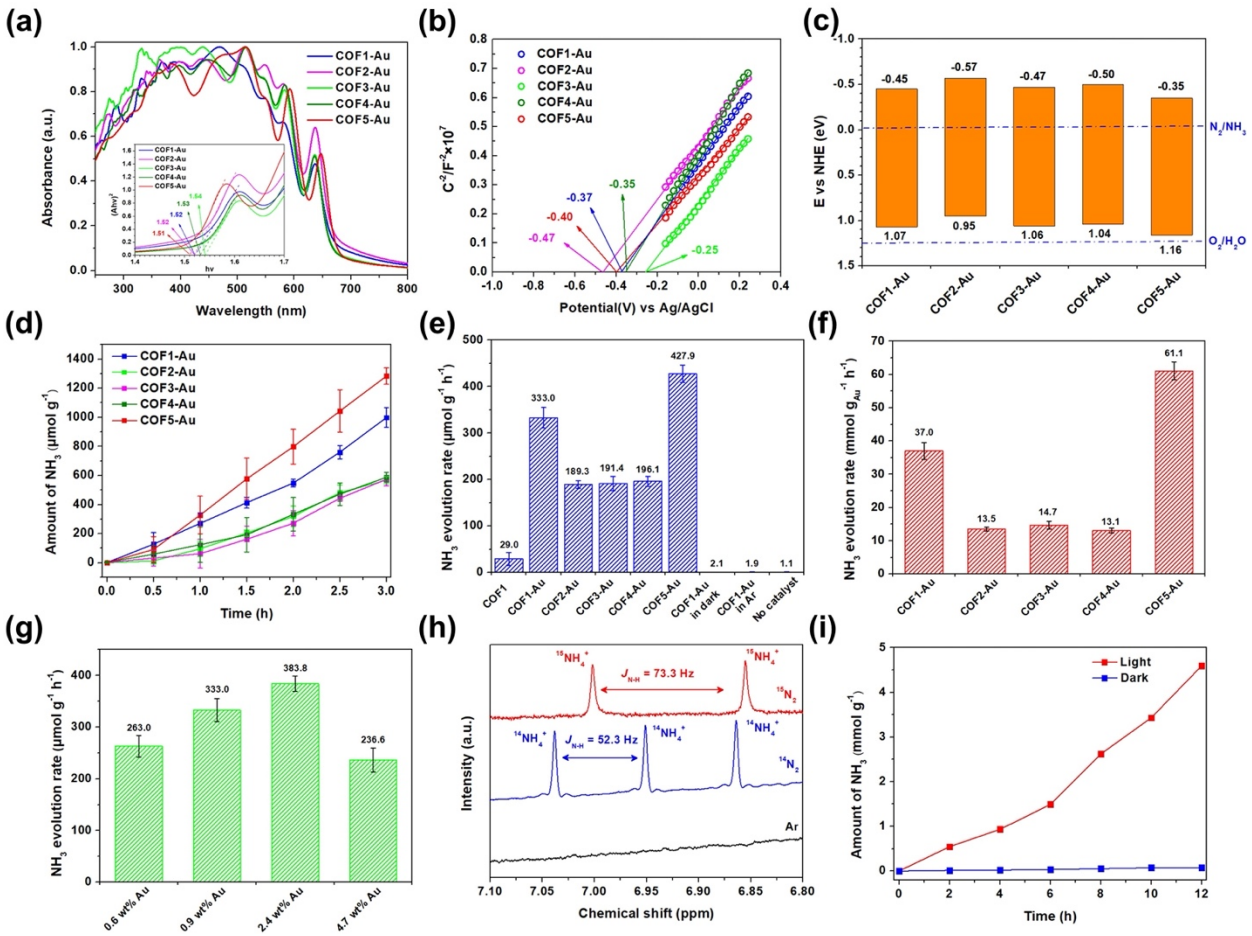


**Figure 5** Photocatalytic $N_2$ fixation. (a) UV-Vis diffuse reflectance spectra (inset: band gaps determined by the Kubelka-Munk-transformed reflectance spectra), (b) Mott-Schottky plots, and (c) band structures of COFX-Au. (d) $NH_3$ evolution curves of COFX-Au monitored over 3 h. (e) $NH_3$ evolution rates of different catalysts in different conditions. (f) $NH_3$ evolution rates of COFX-Au based on the mass of Au. (g) $NH_3$ evolution rates of COF1-Au with

different mass loadings of Au. (h) $^{1}H$ NMR spectra of COF1-Au fed by $^{15}N_2$, $^{14}N_2$ and Ar with full spectrum irradiation. (i) Long-term stability test over COF1-Au.

UV-Vis diffuse reflection absorption spectra presented that COFX exhibited strong absorption in the visible light region with absorption edge extended to 700 nm (Figure S19), which should be originated from the porphyrin units in the frameworks. The COFX-Au did not present obvious changes in their UV-Vis absorption after loading Au single atoms (Figure 5a). The optical band gaps ($E_g$) of COF1-Au, COF2-Au, COF3-Au, COF4-Au, and COF5-Au were calculated to be 1.52, 1.52, 1.53, 1.54, and 1.51 eV (Figure 5a, inset) respectively, by using the Kubelka-Munk equation. The Mott-Schottky plots (Figure 5b) were recorded to determine the flat band potential ($E_{fb}$) of COFX-Au. All five COF/Au systems exhibited positive slopes of the $1/C^2$ versus potential curve, indicating that they are *n*-type semiconductors. The $E_{fb}$ of COF1-Au, COF2-Au, COF3-Au, COF4-Au, and COF5-Au was identified by the intercepts of the curves with the horizontal axis to be -0.35, -0.47, -0.37, -0.40, and -0.25 eV, respectively. As a result, their corresponding conduction band potential ($E_{cb}$) was calculated to be -0.45, -0.57, -0.47, -0.50, and -0.35 eV (Figure 5c). The $E_{cb}$ of COFX-Au was identified to be more negative than the redox potential of $N_2/NH_3$, allowing for the photocatalytic $N_2$ reduction to generate $NH_3$.

Encouraged by the above results, the photocatalytic $N_2$ reduction experiments were conducted with COFX-Au in ultrapure water under irradiation of 300 W xenon lamp, in the presence of $K_2SO_3$ as a sacrificial reagent. The suspension was continuously bubbled with $N_2$ for 30 min before irradiation, and the product was detected by ion chromatography.

Significantly, all COFX-Au samples generated $NH_3$ smoothly over 3 h (Figure 5d) with different evolution rates, revealing that the chemical structures of building blocks showed a remarkable impact on the activity. In particular, when the group at the proximal position of porphyrin units was fixed as hydrogen atom, COF1-Au with benzothiadiazole units (stronger electron-withdrawing group) at the distal position exhibited the highest $NH_3$ evolution rate of 333.0±22.4 μmol $g^{-1}$ $h^{-1}$ (Figure 5e), while COF4-Au with dimethoxybenzene units (stronger electron-donating group) having a similar Au mass loading presented a lower $NH_3$ evolution rate of 196.1±10.8 μmol $g^{-1}$ $h^{-1}$ (Figure 5e) than that of COF1-Au, suggesting that the electron-withdrawing functional groups promoted the $NH_3$ generation. Next, we introduced strong electron-deficient pentafluorobenzene substituents to replace the hydrogen of COF1-Au on proximal position of porphyrin cycle (COF5-Au). The $NH_3$ production rate was increased to 427.9 ± 18.7 μmol $g^{-1}$ $h^{-1}$ (Figure 5e), which further confirmed that the electron-withdrawing groups could facilitate the $NH_3$ production. The $NH_3$ production rates of COF1-Au and COF5-Au were higher than most of reported framework-based materials and conventional photocatalysts (Table S8). $N_2H_4$ was considered as another reduction product from $N_2$. The concentration of $N_2H_4$ was determined by the Watt and Chrisp method.[29] COF1-Au exhibited a low $N_2H_4$ evolution rate of 0.5 μmol $g^{-1}$ $h^{-1}$, revealing its high selectivity (99.9%) toward $NH_3$ (Figure S20). The photocatalytic activity of COF1-Au for water reduction was detected by gas chromatography, and negligible $H_2$ was found under the same conditions with $N_2$ reduction (Figure S21).

The $NH_3$ evolution rates of COFX-Au based on per gram Au (Figure 5f) were also calculated to eliminate the effect of different Au mass loadings. The rates of COF1-Au and

COF5-Au featuring electron-withdrawing groups were calculated to be 37.0±2.5 mmol $g_{Au}^{-1}$ $h^{-1}$ and 61.1±2.7 mmol $g_{Au}^{-1}$ $h^{-1}$, which were about 2.8 and 5.0 times higher than that of COF4-Au equipped with electron-donating functional group, respectively.

To further investigate the role of each counterpart in the photocatalytic reaction, some control experiments were performed. COF1 without Au showed poor activity, with $NH_3$ evolution rate of 29±13.6 μmol $g^{-1}$ $h^{-1}$ (Figure 5e), confirming the high efficiency of Au catalytic centers toward $N_2$ reduction. The reported studies showed that the metal-free pristine COFs with suitable band gaps exhibited photoredox ability for the $H_2O$ reduction or $CO_2$ reduction on account of the semiconducting character.[23] This fact might be the reason why COF1 could produce $NH_3$ with a low generation rate even without the Au catalyst. Negligible $NH_3$ was detected when the experiment was conducted in dark, in argon, or without any catalyst (Figure 5e), revealing that the $NH_3$ production reaction over COF1-Au indeed took place from photocatalytic $N_2$ reduction process. To elucidate the pH effect on the photocatalytic $N_2$ reduction, the pH of catalytic system was adjusted to be 3.95 and 10.03 by using aqueous HCl and potassium hydroxide, respectively. COF1-Au exhibited comparable $NH_3$ production performance with a rate of 168.6 μmol $g^{-1}$ $h^{-1}$ in acidic $K_2SO_3$ aqueous solution (pH = 3.95, Figure S22). Surprisingly, basic solution greatly suppressed the $N_2$ reduction with only a $NH_3$ generation rate of 7.8 μmol $g^{-1}$ $h^{-1}$ for COF1-Au (Figure S22).

To further investigate the roles of COF crystalline structures and Au catalytic centers, a molecular catalyst, 5,5'-(porphyrin-5,15-diyl)diisophthalaldehyde-gold (P-CHO-Au, 86% porphyrin units were metalized by Au according to the ICP and MALDI-TOF results, see the Supporting Information for the synthesis details), was synthesized in addition to P-Au. The

$NH_3$ evolution rates of P-Au and P-CHO-Au were determined to be 0.216 and 0.470 mmol $g_{Au}^{-1}$ $h^{-1}$, which were 283-fold and 130-fold lower than that of COF5-Au, respectively (Figure S23). The crystalline and porous structures of COFs remarkably boosted the $NH_3$ generation rates compared to the molecular catalysts. Furthermore, P-CHO-Au decorated with aldehyde groups presented higher $NH_3$ evolution rate than that of P-Au, indicating that the activity of Au catalytic centers could be increased through tuning the chemical structures around porphyrin units. 5,5'-(Porphyrin-5,15-diyl)diisophthalaldehyde (P-CHO) without Au species was also determined with negligible $NH_3$ generation (Figure S23), confirming the catalytic nature of Au atoms during the photocatalytic $N_2$ reduction process.

Interestingly, the $NH_3$ evolution rate demonstrated a volcano-like trend, with a highest rate of 383.8±15 μmol $g^{-1}$ $h^{-1}$ (Figure 5g) over 2.4 wt% Au. The lower activity of COF1-Au with 4.7 wt% mass loading was ascribed to the formation of Au particles, as confirmed by PXRD and TEM measurements (Figures S24 and S25). The result further illuminated the advantage of single-atom catalytic centers.

The $^{15}N_2$ isotope labeling experiments based on COF1-Au were performed to verify that the $NH_3$ was indeed produced from the $N_2$ gas rather than COF skeletons. As shown in Figure 5h, the reacted solution with $^{15}N_2$ exhibited the doublets of $^{15}NH_4^+$ having a coupling constant of 73.3 Hz, while the triplets of $^{14}NH_4^+$ with a coupling constant of 52.3 Hz was achieved when using $^{14}N_2$ gas, confirming that the detected $NH_3$ was originated from $N_2$. No nitrogen signal was detected when the mixture was bubbled with Ar. The same conclusion was achieved with COF5-Au (Figure S26), further confirming that $NH_3$ was originated from $N_2$ feed gas. The apparent quantum yield (AQY) based on COF1-Au was investigated under the

irradiation of monochromatic light with specific wavelength to quantify the spectral contribution for the $NH_3$ production. The AQY of COF1-Au was measured to be 0.08, 0.22 and 0.29 % at 402, 420 and 455 nm, respectively (Figure S27).

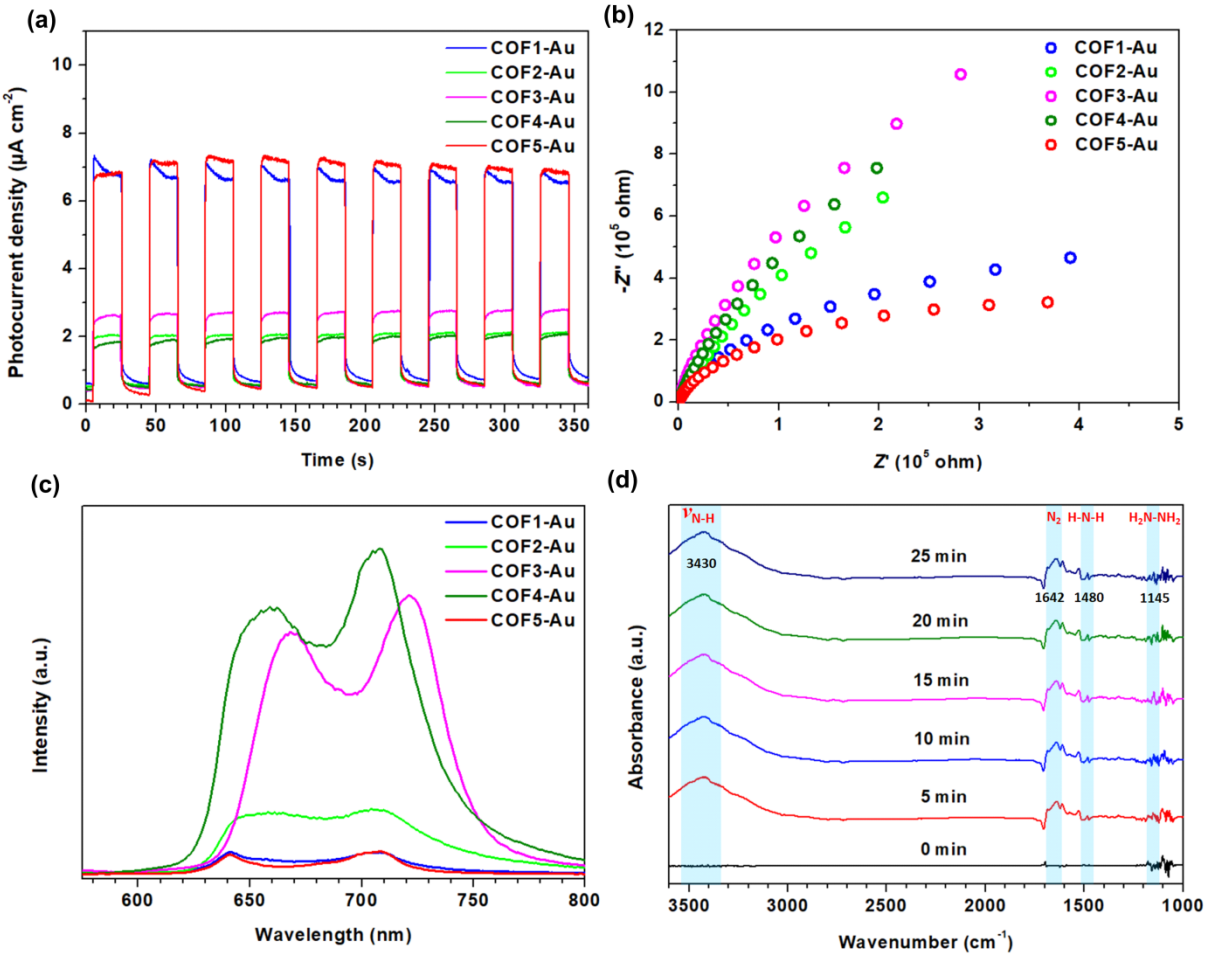


**Figure 6** Photoelectrochemical property. (a) Photocurrent responses, (b) EIS Nyquist plots, and (c) PL emission spectra of COFX-Au. (d) In situ FTIR spectra recorded during the photocatalytic $NH_3$ synthesis over COF1-Au.

The stability of photocatalysts was evaluated through carrying out the long-term photocatalytic experiments. Both COF1-Au (Figure 5i) and COF5-Au (Figure S28) with electron-withdrawing groups exhibited steady photocatalytic activity over a 12 h continuous irradiation. The PXRD curve (Figure S29) and TEM image (Figure S30) demonstrated that

COFX-Au maintained its crystallinity and morphology after the photocatalytic reaction.

To further acquire an insight into the role of chemical structures in improving the activity, photoelectrochemical experiments were carried out. The photocurrent response curves (Figure 6a) of COF1-Au and COF5-Au exhibited much higher photocurrent density than the other three photocatalysts, suggesting that the introduction of strong electron-withdrawing functional groups was beneficial for the improvement of charge separation efficiency for COF photocatalysts.[30] In addition, the electrochemical impedance spectra (EIS) of COF5-Au displayed the smallest arc radius of Nyquist curve (Figure 6b), indicating the lowest charge transfer resistance. The steady-state and time-resolved photoluminescence (PL) spectra of COFX-Au were recorded to further explore the electron-transfer behavior. There were two separated peaks at 640-680 and 690-730 nm in the steady-state PL spectra of COFX-Au (Figure 6c), which were in line with reported porphyrin-based porous materials.[13,31] COF1-Au and COF5-Au demonstrated much lower PL intensity than other catalysts (Figure 6c), revealing the effective suppression of charge carrier recombination in electron-withdrawing COF systems.[14] The average fluorescence lifetime of COF1-Au, COF2-Au, COF3-Au, COF4-Au and COF5-Au was calculated to be 0.92, 0.73, 0.78, 0.69 and 1.02 ns according to the time-resolved PL spectra, respectively (Figure S31). As the recombination of photogenerated charge carriers could decrease the photocatalytic efficiency, the longest fluorescence lifetime of COF5-Au led to the best photocatalytic $N_2$ reduction performance.[32]

Time-dependent in situ FTIR experiments (Figure 6d) were performed to investigate the $N_2$ activation in the photocatalytic $N_2$ reduction. The peak at 1642 $cm^{-1}$ appeared quickly due to the fast adsorption of $N_2$ on the surface of catalysts.[10] The activation of $N_2$ led to the

formation of N−H stretching vibration[33] at 3430 $cm^{-1}$. The two peaks at 1480 and 1145 $cm^{-1}$ were detected as the H−N−H bending vibration and $H_2N-NH_2$ stretching vibration from intermediate products, respectively.[7] Moreover, the intensity of peaks increased gradually along with the irradiation time, revealing that the $N_2$ reduction reaction took place smoothly.

The photocatalytic $N_2$ reduction reaction pathways of photocatalysis should involve the photoexcitation, separation and transportation of photogenerated charge carriers and redox reactions in addition to the activation of $N_2$. As a preliminary trail of understanding the effect of functional groups at the proximal position, we used DFT methods to calculate the binding energy of $N_2$ ($\Delta G_{N_2}{}^*$) adsorbing on porphyrin-Au models (Figure S32). The $\Delta G_{N_2}{}^*$ of pentafluorobenzene decorated porphyrin-Au was calculated to be 0.29 eV, which was lower than that of bare porphyrin-Au (0.33 eV). The results implied that the strong electron-withdrawing functional groups facilitated the adsorption of $N_2$ on the Au catalytic centers.

## Conclusion

In conclusion, we have prepared five isostructural porphyrin-based COFs with high crystallinity and porosity. The porphyrin macrocycles act as molecular docking sites to immobilize Au species as single atoms. Interestingly, the microenvironment of Au catalytic centers is precisely tuned through changing the functional groups at the proximal and distal positions of porphyrins *via* modular design strategy. The as-prepared COFX-Au photocatalysts displays excellent $NH_3$ evolution performance in photocatalytic $N_2$ reduction along with excellent stability. Moreover, COF1-Au and COF5-Au decorated with

electron-withdrawing groups exhibit higher $NH_3$ production rates of 333.0±22.4 and 427.9± 18.7 μmol $g^{-1}$ $h^{-1}$ respectively, compared to COF2-Au, COF3-Au and COF4-Au. The superior performance of photocatalysts decorated with electron-withdrawing groups is ascribed to the higher charge separation efficiency and lower charge transfer resistance. This study provides a guidance for the precise design of advanced COF catalysts toward photocatalytic $N_2$ fixation.

**Experimental Section**

**COF1.** An *o*-DCB/*n*-BuOH (*v*/*v* = 1/1, 1 mL) mixture containing P-CHO (11.5 mg, 0.02 mmol) and Bt-$NH_2$ (12.7 mg, 0.04 mmol) in the presence of acetic acid (6M, 0.1 mL) was added in a 10 mL Pyrex tube. Then, the system was degassed by three freeze-pump-thaw cycles. The sealed tube was treated at 120 °C for three days. The red solid was obtained by filtration, washed with THF, and purified by Soxhlet extraction with THF for 24 h. COF1 was collected and dried at room temperature under vacuum overnight in 88 % yield.

**COF2.** An *o*-DCB/ethanol (*v*/*v* = 1/1, 1 mL) mixture of P-CHO (11.5 mg, 0.02 mmol) and Pz-$NH_2$ (10.5 mg, 0.04 mmol) in the presence of acetic acid (6M, 0.1 mL) was added in a 10 mL Pyrex tube. The following procedures were similar to the preparation of COF1. COF2 was collected and dried at room temperature under vacuum overnight in 82 % yield.

**COF3.** An *o*-DCB/*n*-BuOH (*v*/*v* = 1/1, 1 mL) mixture of P-CHO (11.5 mg, 0.02 mmol) and TP-$NH_2$ (10.4 mg, 0.04 mmol) in the presence of acetic acid (6M, 0.1 mL) was added in a 10 mL Pyrex tube. The following procedures were similar to the preparation of COF1. COF3 was collected and dried at room temperature under vacuum overnight in 88 % yield.

**COF4.** An *o*-DCB/*n*-BuOH (*v*/*v* = 1/1, 1 mL) mixture of P-CHO (11.5 mg, 0.02 mmol) and

DMTP-$NH_2$ (12.8 mg, 0.04 mmol) in the presence of acetic acid (6M, 0.1 mL) was added in a 10 mL Pyrex tube. The following procedures were similar to the preparation of COF1. COF4 was collected and dried at room temperature under vacuum overnight in 85 % yield.

**COF5.** An *o*-DCB/*n*-BuOH (*v*/*v* = 1/1, 1 mL) mixture of $PF_5$-CHO (18.1 mg, 0.02 mmol) and Bt-$NH_2$ (12.7 mg, 0.04 mmol) in the presence of TFA (0.7M, 0.1 mL) was added in a 10 mL Pyrex tube. The following procedures were similar to the preparation of COF1. COF5 was collected and dried at room temperature under vacuum overnight in 80 % yield.

**COFX-Au.** A mixture of COFX (20 mg), $KAuCl_4$ aqueous solution (100 μL, 100 mg/mL) and DMF (3 mL) was added into a 10 mL Schlenk tube. The mixture was sonicated for 10 min and then stirred at 85 °C for 24 h. The precipitate was collected by centrifugation at 8,000 rpm for 5 min and washed with THF for three times. The resulting COFX-Au was dried at room temperature under vacuum overnight. For COF1-Au with different amounts of Au mass loading, $KAuCl_4$ aqueous solution (50 μL, 200 μL, and 400 μL, 100 mg/mL) was added to the mixture to generate COF1-Au with 0.6 wt%, 2.4 wt% and 4.7 wt% loading, respectively.

**Photocatalytic $NH_3$ Evolution.** Typically, the catalyst (10 mg) was dispersed in ultrapure water (100 mL) with $K_2SO_3$ (16 mg) in a quartz reactor. The suspension was then bubbled with nitrogen to remove the residual oxygen in the dark. The photocatalytic $NH_3$ evolution experiment was carried out by irradiating the mixture with a 300-W Xenon lamp (power density of 172 mW $cm^{-2}$). The amount of $NH_3$ was measured by analyzing 5 mL reaction liquid with ion chromatography.

## ASSOCIATED CONTENT

## Supporting Information

This material is available free of charge via the Internet at http://pubs.acs.org.

Methods and materials, synthetic procedures and characterization, schematic illustration, thermogravimetric analysis curves, FTIR spectra, nitrogen sorption curves and pore size distribution, SEM and TEM images, PXRD patterns, aberration-corrected HAADF-STEM image, UV-Vis diffuse reflectance spectra, UV-Vis absorption spectra and calibration curves, $NH_3$ evolution rates, $^1H$ NMR spectra, apparent quantum yields, transient fluorescence lifetime decay curves, molecular models, atomic coordinates, EXAFS fitting curve, photocatalytic activity, and experimental appendix.

## AUTHOR INFORMATION


### Corresponding Author

* zhaoyanli@ntu.edu.sg; zhyjiang@tju.edu.cn.


### Author Contributions

¥These authors contributed equally to this work.


### Acknowledgements

Y. Z. thanks for the support from the Ministry of Education Singapore under its Academic Research Funds (RG3/21, MOE2019-T2-2-049 and MOET2EP10120-0003) and the Singapore Agency for Science, Technology and Research (A*STAR) under the Manufacturing, Trade and Connectivity Individual Research Grant (M21K2c0105). Z. J.

acknowledges the economic support from the National Natural Science Foundation of China (21621004). X. L. and H.-J. P. acknowledge the support of National Natural Science Foundation of China (22109020 and 22109082). The authors acknowledge the support of NTU Center of High Field NMR Spectroscopy and Imaging for characterization. The computational work for this article was partially performed on resources of the National Supercomputing Centre, Singapore (https://www.nscc.sg).

**References**

(1) Chalkley, M. J.; Drover, M. W.; Peters, J. C. Catalytic $N_2$-to-$NH_3$ (or -$N_2H_4$) Conversion by Well-Defined Molecular Coordination Complexes. *Chem. Rev.* **2020**, *120*, 5582−5636.

(2) Chen, J. G.; Crooks, R. M.; Seefeldt, L. C.; Bren, K. L.; Bullock, R. M.; Darensbourg, M. Y.; Holland, P. L.; Hoffman, B.; Janik, M. J.; Jones, A. K.; Kanatzidis, M. G.; King, P.; Lancaster, K. M.; Lymar, S. V.; Pfromm, P.; Schneider, W. F.; Schrock, R. R. Beyond Fossil Fuel Driven Nitrogen Transformations. *Science* **2018**, *360*, eaar6611.

(3) Suryanto, B.; Du, H.; Wang, D.; Chen, J.; Simonov, A.; MacFarlane, D. Challenges and Prospects in the Catalysis of Electroreduction of Nitrogen to Ammonia. *Nat. Catal.* **2019**, *2*, 290−296.

(4) Fryzuk, M. D. More can be Better in $N_2$ Activation. *Science* **2013**, *340*, 1530−1531.

(5) Chen, L.; Hao, Y.; Guo, Y.; Zhang, Q.; Li, J.; Gao, W.; Ren, L.; Su, X.; Hu, L.; Zhang, N.; Li, S.; Feng, X.; Gu, L.; Zhang, Y.; Yin, A.; Wang, B. Metal-Organic Framework Membranes Encapsulating Gold Nanoparticles for Direct Plasmonic Photocatalytic Nitrogen Fixation. *J. Am. Chem. Soc.* **2021**, *143*, 5727−5736.

(6) Guo, B.; Cheng, X.; Tang, Y.; Guo, W.; Deng, S.; Wu, L.; Fu, X. Dehydrated UiO-66(SH)$_2$: The Zr−O Cluster and Its Photocatalytic Role Mimicking the Biological Nitrogen Fixation. *Angew. Chem. Int. Ed.* **2022**, *61*, e202117244.

(7) Zhao, Z.; Ren, H.; Yang, D.; Han, Y.; Shi, J.; An, K.; Chen, Y.; Shi, Y.; Wang, W.; Tan, J.; Xin, X.; Zhang, Y.; Jiang, Z. Boosting Nitrogen Activation *via* Bimetallic Organic Frameworks for Photocatalytic Ammonia Synthesis. *ACS Catal.* **2021**, *11*, 9986−9995.

(8) Hu, K.; Qiu, P.; Zeng, L.; Hu, S.; Mei, L.; An, S.; Huang, Z.; Kong, X.; Lan, J.; Yu, J.; Zhang, Z.; Xu, Z.; Gibson, J.; Chai, Z.; Bu, Y.; Shi, W. Solar-Driven Nitrogen Fixation Catalyzed by Stable Radical Containing MOFs: Improved Efficiency Induced by a Structural Transformation. *Angew. Chem. Int. Ed.* **2020**, *59*, 20666–20671.

(9) Brown, K. A.; Harris, D. F.; Wilker, M. B.; Rasmussen, A.; Khadka, N.; Hamby, H.; Keable, S.; Dukovic, G.; Peters, J. W.; Seefeldt, L. C.; King, P. W. Light-Driven Dinitrogen Reduction Catalyzed by a CdS: Nitrogenase MoFe Protein Biohybrid. *Science* **2016**, *352*, 448−450.

(10) Li, P.; Zhou, Z.; Wang, Q.; Guo, M.; Chen, S.; Low, J.; Long, R.; Liu, W.; Ding, P.; Wu, Y.; Xiong, Y. Visible-Light-Driven Nitrogen Fixation Catalyzed by $Bi_5O_7Br$ Nanostructures: Enhanced Performance by Oxygen Vacancies. *J. Am. Chem. Soc.* **2020**, *142*, 12430−12439.

(11) Wang, Z.; Hu, X.; Liu, Z.; Zou, G.; Wang, G.; Zhang, K. Recent Developments in Polymeric Carbon Nitride-Derived Photocatalysts and Electrocatalysts for Nitrogen Fixation. *ACS Catal.* **2019**, *9*, 10260−10278.

(12) Ji, S.; Chen, Y.; Wang, X.; Zhang, Z.; Wang, D.; Li, Y. Chemical Synthesis of Single Atomic Site Catalysts. *Chem. Rev.* **2020**, *120*, 11900−11955.

(13) Shang, S.; Xiong, W.; Yang, C.; Johannessen, B.; Liu, R.; Hsu, H.; Gu, Q.; Leung, M. K. H.; Shang, J. Atomically Dispersed Iron Metal Site in a Porphyrin-Based Metal−Organic Framework for Photocatalytic Nitrogen Fixation. *ACS Nano* **2021**, *15*, 9670–9678.

(14) He, T.; Chen, S.; Ni, B.; Gong, Y.; Wu, Z.; Song, L.; Gu, L.; Hu, W.; Wang, X. Zirconium–Porphyrin-Based Metal–Organic Framework Hollow Nanotubes for Immobilization of Noble-Metal Single Atoms. *Angew. Chem. Int. Ed.* **2018**, *57*, 3493–3498.

(15) Zhang, B.; Zhang, J.; Shi, J.; Tan, D.; Liu, L.; Zhang, F.; Lu, C.; Su, Z.; Tan, X.; Cheng, X.; Han, B.; Zheng, L.; Zhang, J. Manganese Acting as a High-Performance Heterogeneous Electrocatalyst in Carbon Dioxide Reduction. *Nat. Commun.* **2019**, *10*, 2980.

(16) Zhao, X.; Huang, S.; Chen, Z.; Lu, C.; Han, S.; Ke, C.; Zhu, J.; Zhang, J.; Tranca, D.; Zhuang, X. Carbon Nanosheets Supporting Ni–$N_3S$ Single-Atom Sites for Efficient Electrocatalytic $CO_2$ Reduction. *Carbon* **2021**, *178*, 488–496.

(17) Yang, D.; Ni, B.; Wang, X. Heterogeneous Catalysts with Well-Defined Active Metal Sites toward $CO_2$ Electrocatalytic Reduction. *Adv. Energy Mater.* **2020**, *10*, 2001142.

(18) Diercks, C. S.; Yaghi, O. M. The Atom, the Molecule, and the Covalent Organic Framework. *Science* **2017**, *355*, eaal1585.

(19) Geng, K.; He, T.; Liu, R.; Dalapati, S.; Tan, K. T.; Li, Z.; Tao, S.; Gong, Y.; Jiang, Q.; Jiang, D. Covalent Organic Frameworks: Design, Synthesis, and Functions. *Chem. Rev.* **2020**, *120*, 8814–8933.

(20) He, T.; Geng, K.; Jiang, D. All $sp^2$ Carbon Covalent Organic Frameworks. *Trends Chem.* **2021**, *3*, 431−444.

(21) Gropp, C.; Ma, T.; Hanikel, N.; Yaghi, O. M. Design of Higher Valency in Covalent Organic Frameworks. *Science* **2020**, *370*, eabd6406.

(22) Qian, C.; Zhou, W.; Qiao, J.; Wang, D.; Li, X.; Teo, W. L.; Shi, X.; Wu, H.; Di, J.; Wang, H.; Liu, G.; Gu, L.; Liu, J.; Feng, L.; Liu, Y.; Quek, S. Y.; Loh, K. P.; Zhao, Y. L. Linkage Engineering by Harnessing Supramolecular Interactions to Fabricate 2D Hydrazone-Linked Covalent Organic Framework Platforms toward Advanced Catalysis. *J. Am. Chem. Soc.* **2020**, *142*, 18138−18149.

(23) Wang, H.; Wang, H.; Wang, Z.; Tang, L.; Zeng, G.; Xu, P.; Chen, M.; Xiong, T.; Zhou, C.; Li, X.; Huang, D.; Zhu, Y.; Wang, Z.; Tang, J. Covalent Organic Framework Photocatalysts: Structures and Applications. *Chem. Soc. Rev.* **2020**, *49*, 4135–4165.

(24) Wang, X.; Chen, L.; Chong, S. Y.; Little, M. A.; Wu, Y.; Zhu, W.; Clowes, R.; Yan, Y.; Zwijnenburg, M. A.; Sprick, R. S.; Cooper, A. I. Sulfone-Containing Covalent Organic Frameworks for Photocatalytic Hydrogen Evolution from Water. *Nat. Chem.* **2018**, *10*, 1180–1189.

(25) Keller, N.; Bein, T. Optoelectronic Processes in Covalent Organic Frameworks. *Chem. Soc. Rev.* **2021**, *50*, 1813–1845.

(26) Li, Z.; He, T.; Gong, Y.; Jiang, D. Covalent Organic Frameworks: Pore Design and Interface Engineering. *Acc. Chem. Res.* **2020**, *53*, 1672–1685.

(27) Zhang, J.; Liu, J.; Xi, L.; Yu, Y.; Chen, N.; Sun, S.; Wang, W.; Lange, K. M.; Zhang, B. Single-Atom Au/NiFe Layered Double Hydroxide Electrocatalyst: Probing the Origin of Activity for Oxygen Evolution Reaction. *J. Am. Chem. Soc.* **2018**, *140*, 3876−3879.

(28) Yang, D.; Yu, H.; He, T.; Zuo, S.; Liu, X.; Yang, H.; Ni, B.; Li, H.; Gu, L.; Wang, D.; Wang, X. Visible-Light-Switched Electron Transfer over Single Porphyrin-Metal Atom Center for Highly Selective Electroreduction of Carbon Dioxide. *Nat. Commun.* **2019**, *10*, 3844.

(29) Shi, M.; Bao, D.; Wulan, B.; Li, Y.; Zhang, Y.; Yan, J.; Jiang, Q. Au Sub-Nanoclusters on $TiO_2$ toward Highly Efficient and Selective Electrocatalyst for $N_2$ Conversion to $NH_3$ at Ambient Conditions. *Adv. Mater.* **2017**, *29*, 1606550.

(30) Guo, S.; Bu, K.; Li, J.; Hu, Q.; Luo, H.; He, Y.; Wu, Y.; Zhang, D.; Zhao, Y.; Yang, W.; Kanatzidis, M. G.; Lü, X. Enhanced Photocurrent of All-Inorganic Two-Dimensional Perovskite $Cs_2PbI_2Cl_2$ *via* Pressure-Regulated Excitonic Features. *J. Am. Chem. Soc.* **2021**, *143*, 2545–2551.

(31) Fang, X.; Shang, Q.; Wang, Y.; Jiao, L.; Yao, T.; Li, Y.; Zhang, Q.; Luo, Y.; Jiang, H. L. Single Pt Atoms Confined into a Metal Organic Framework for Efficient Photocatalysis. *Adv. Mater.* **2018**, *30*, 1705112.

(32) Wu, Y.; Shi, J.; Li, D.; Zhang, S.; Gu, B.; Qiu, Q.; Sun, Y.; Zhang, Y.; Cai, Z.; Jiang, Z. Synergy of Electron Transfer and Electron Utilization *via* Metal-Organic Frameworks as an Electron Buffer Tank for Nicotinamide Regeneration. *ACS Catal.* **2020**, *10*, 2894−2905.

(33) Dong, G.; Qiu, P.; Chen, Q.; Huang, C.; Chen, F.; Liu, X.; Li, Z.; Wang, Y.; Zhao, Y. $K^+$-Intercalated Carbon Nitride with Electron Storage Property for High-Efficiency Visible Light Driven Nitrogen Fixation. *Chem. Eng. J.* **2022**, *433*, 133573.

## Table of Contents Graphic